Journal of Materials Chemistry C

ROYAL SOCIETY OF CHEMISTRY

PAPER

View Article Online
View Journal | View Issue

Cite this: J. Mater. Chem. C, 2025, 13, 17101

High mobility field-effect transistors produced by direct growth of C_{70} single crystals from a solution†

Yuto Sakai,[a] Taiyo Araki,[a] Ryo Suzuki,[a] Toshiyuki Sasaki,[b] Kouhei Ichiyanagi,[b] Tadahiko Hirai,[c] Nobuyuki Aoki[d] and Masaru Tachibana *[a]

Received 23rd April 2025,
Accepted 2nd July 2025

DOI: 10.1039/d5tc01627d

rsc.li/materials-c

Fullerene C_{70} crystals are n-type semiconductor materials that are used in organic field-effect transistors (OFETs). However, research on C_{70} FETs has so far been limited to low electron mobilities below $\sim 10^{-2}$ cm^2 V^{-1} s^{-1}. To achieve higher mobilities, it is essential to enhance the electrical contact between C_{70} crystals and the FET substrate with electrodes, as well as to grow high-quality crystals. In this study, high-mobility FETs were produced by directly growing C_{70} crystals from a C_{70} saturated *m*-xylene solution. Good electrical contact between the C_{70} crystals and FET substrates with electrodes is realized in a bottom-gated bottom-contact FET configuration. The resulting rhombohedral shaped C_{70} crystals exhibited solvated hexagonal structures with lattice parameters of a = 50.52 Å and c = 24.70 Å. These directly grown C_{70} crystal FETs exhibited typical n-type output and transfer characteristics. The electron mobility improved after annealing at 100 °C in a vacuum, which is probably due to the desorption of H_2O and O_2 in the crystals, although the solvation in the crystals was preserved. The solvated C_{70} crystal FETs achieved a high electron mobility of 1.14 cm^2 V^{-1} s^{-1} which is an improvement of more than two orders of magnitude relative to previously documented C_{70} FETs, demonstrating the potential of C_{70} crystals for use in electronic devices.

Introduction

Fullerene C_{60} and C_{70} crystals are n-type semiconductor materials.[1,2] Among them, C_{60} crystals have been extensively studied for use in organic field-effect transistors (OFETs). The electron mobility of C_{60}-based FETs is 0.08–3.23 cm^2 V^{-1} s^{-1} in thin-film devices[1,3–6] and 0.002–0.0382 cm^2 V^{-1} s^{-1} in single-crystal devices.[7–11] These FETs are typically fabricated in a bottom-contact configuration. In contrast, top-contact configurations have achieved higher mobilities of over 1 cm^2 V^{-1} s^{-1} in both FETs based on thin films[5,12,13] and C_{60} single-crystal needles aligned by controlled growth.[14–17] The highest reported electron mobility is 11 cm^2 V^{-1} s^{-1},[14] placing C_{60} among the most promising n-type semiconductors.[18]

C_{70} has a similar electronic state to C_{60}, although the lowest unoccupied molecular orbital (LUMO) energy level of C_{70} is slightly lower than that of C_{60}.[10,11,19–21] The lower LUMO level of C_{70} compared to that of C_{60} may reduce the energy barrier for electron injection from electrodes, when gold is used as an electrode in FETs, as previously reported. Therefore, C_{70} is expected to exhibit superior FET performance, similar to that of C_{60}. However, studies on OFETs based on C_{70} are limited to thin films with low crystallinity, owing to the difficulty in growing high-quality single crystals. Moreover, the electron mobility in thin C_{70} films is 0.002–0.066 cm^2 V^{-1} s^{-1},[2,4] which is relatively low compared to that of C_{60}.

Studies on C_{70} FETs using single crystals with a bottom-contact configuration have also been conducted. However, the measured value for electron mobility was $\sim 10^{-5}$ cm^2 V^{-1} s^{-1},[20–22] which is lower than that of the aforementioned thin C_{70} films. Even C_{70} FETs using needle-like single crystals have a maximum electron mobility of only 1.32 × 10^{-2} cm^2 V^{-1} s^{-1},[23] which is comparable to that of thin films. As for the output characteristics of the C_{70} needle crystal FETs, the drain current slowly increased with the drain voltage in the low-voltage region. Moreover, no clear saturation of the drain current was observed, even at higher voltages. This behavior can be attributed to the poor or non-ohmic contact between the C_{70} crystal and the FET substrate with the electrodes. In these devices, C_{70} needle

[a] Department of Materials System Science, Yokohama City University, 22-2 Seto, Kanazawa-ku, Yokohama 236-0027, Japan. E-mail: tachiban@yokohama-cu.ac.jp
[b] Japan Synchrotron Radiation Research Institute, 1-1-1 Kouto, Sayo-cho, Sayo-gun, Hyogo 679-5198, Japan
[c] CSIRO Manufacturing, Research Way Clayton, Victoria 3168, Australia
[d] Department of Materials Science, Chiba University, 1-33 Yayoi-cho, Inage-ku, Chiba 263-8522, Japan

† Electronic supplementary information (ESI) available. See DOI: https://doi.org/10.1039/d5tc01627d

crystals grown in solution were simply dropped and dried onto the FET substrate to bridge the source and drain electrodes.

To achieve enhanced FET characteristics and higher electron mobility, the electrical contact between the C_{70} crystals and the FET substrates with the electrodes has to be improved. The top-contact configuration in FET devices is useful to improve the electrical contact. However, fabrication of the top-contact configuration is difficult owing to the small size of the C_{70} crystals. In addition, the C_{70} crystals can be damaged at high temperatures when metal electrodes are thermally deposited on the crystals in the top-contact configuration. In this paper, a high-mobility FET fabricated by direct growth of C_{70} crystals from a solution for improved electrical contact in a bottom-contact configuration is reported.

Solution processing techniques such as drop casting, solution shearing, dip coating, spin coating and printing techniques have previously been used successfully for the fabrication of high-mobility organic crystal FETs.[24,25] In this work, a simple solution evaporation method was applied for the fabrication of C_{70} single crystal FETs for the first time. The solvated C_{70} crystal FETs exhibited electron mobility that was more than two orders of magnitude higher than that reported for previous C_{70} FETs, highlighting the potential of C_{70} crystals for electronic applications.

Experimental

Crystallization and characterization

A solution evaporation method was used for direct crystal growth on the FET substrate. The solution used was *m*-xylene saturated with C_{70} (C_{70}-*m*-xylene). To optimize the crystallization conditions, crystals were grown under various conditions, such as varying amounts and temperature of the solution and evaporation time. C_{70} crystals with rhombohedral shapes and clear crystal behavior are commonly obtained under various conditions, although the size and number of crystals obtained depend on the growth conditions. Fig. S1 (ESI†) shows C_{70} crystals with rhombohedral shapes grown on the SiO_2–Si substrate. This study focused on C70 crystals with rhombohedral shapes as they are more stable compared to other needle crystals.

The morphology and size of the solution-grown C_{70} crystals were observed by optical microscopy (BX51, OLYMPUS) and scanning electron microscopy (SEM, S-4300, HITACHI). The crystal structure of the C_{70} crystals with rhombohedral shapes was determined by powder X-ray diffraction (PXRD) with Cu-Kα radiation (λ = 1.5418 Å) (D8-ADVANCE, BRUKER) and single crystal X-ray diffraction (SCXRD) at SPring-8 (BL40XU) with synchrotron radiation (λ = 0.81 Å). For SCXRD, the crystal data were collected at 100 K with a detector distance of 50.5 mm, a chi value of 45°, a 2θ value of 25°, an omega range from −90° to 90°, a delta omega value of 0.2°, and phi values of 0°, 90°, 180°, and 270°. Data integration was performed using CrysAlisPro software (Rigaku OD, 2024). The chemical composition was confirmed by Fourier-transform infrared spectroscopy (FT-IR, FT/IR-410, JASCO) with an attenuated total reflection prism (ATR PRO ONE, JASCO). It was also confirmed by thermogravimetric (TG) analysis (STA7300, HITACHI) at a heating rate of 10 °C min^{-1} in air, where the heating temperature was 25 to 600 °C.

FET device fabrication

FETs with rhombohedral shaped C_{70} crystals were constructed in a bottom-gated bottom-contact configuration. An n^{++}–Si wafer with a thermally grown SiO_2 insulating layer (300 nm) was used as the substrate. Interdigital array electrodes of the Au/Cr (40/10 nm) source and drain were fabricated by photolithography on the surface of SiO_2. An FET substrate with electrodes was used to fabricate the C_{70} crystal FETs.

A schematic representation of the FET substrate with the electrodes is shown in Fig. S2 in the ESI.†

C_{70} crystals with rhombohedral shapes were grown directly on FET substrates with electrodes. The FET fabrication procedure is shown schematically in Fig. S3 (see the ESI†). First, the FET substrate was sequentially washed with acetone, IPA, and distilled water for 2 min each. If dirt remained, washing was repeated with IPA and distilled water. The FET substrate was further irradiated with a UV lamp (UV253MINI R, Filgen) for 25 min to remove impurities.

The cleaned FET substrate was placed in a Petri dish (diameter: 3 cm). Subsequently, 0.7 mL C_{70} *m*-xylene solution was injected into the Petri dish. The Petri dish was then partially covered with a plate and kept for 30 min at 20 °C. By partially covering the Petri dish, the evaporation of the solvent can be controlled so that the number of nucleation sites for crystallization can be suppressed.

The crystallized FET substrate was then removed from the Petri dish and allowed to dry naturally in air. Consequently, some C_{70} crystals with rhombohedral shapes were then grown directly on the FET substrate. Crystallization occurs preferentially at the step edges of the electrodes on the FET substrate, as shown in Fig. S4 (ESI†). Thus, some C_{70} crystals with rhombohedral shapes could be successfully grown between the electrodes. The electrical properties of the obtained FETs with the rhombohedral C_{70} crystals were measured.

Current–voltage measurements

Current–voltage measurements were performed under 3.0–4.0 × 10^{-3} Pa in the dark using a semiconductor parameter analyzer (B1500A, KEYSIGHT). To remove the adsorbed H_2O and O_2, the fabricated device was annealed at 100 °C under 3.0–4.0 × 10^{-3} Pa for approximately 25 days. The FET characteristics were evaluated without exposing the devices to the ambient atmosphere.

The electron mobility was calculated as follows:

$$\mu = \frac{2L}{WC}\left(\frac{\partial\sqrt{I_{DS}}}{\partial V_G}\right)^2,$$

where μ is the electron mobility, L is the average length of the contact region with the insulating layer, W is the total width of the crystals on the FET substrate, C is the electrical capacity of

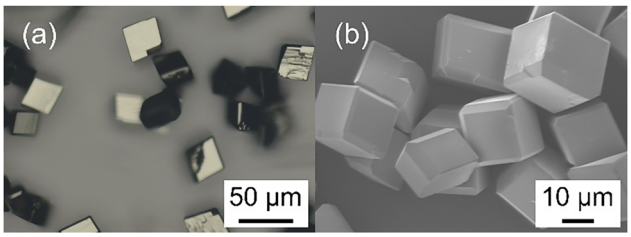

Fig. 1 (a) Optical micrograph and (b) SEM image of rhombohedral shaped C_{70} crystals grown from a C_{70}-*m*-xylene solution.

the insulating layer, I_{DS} is the source–drain current, and V_G is the gate voltage. W and L were measured using scanning electron microscopy (SEM), as shown in Fig. 1. W is defined as

$$W = \frac{W_1 + W_2}{2}.$$

Results and discussion

Solution-grown C_{70} crystals

To determine the structure and composition of C_{70} crystals with rhombohedral shapes, many crystals were grown using the solvent evaporation method. The crystals obtained had rhombohedral shapes with clear crystal habits (Fig. 1), although the size and number of crystals depended on the amount and temperature of the solution and the evaporation time. Fig. S5 (ESI†) shows optical micrographs of C_{70} crystals from different saturated solutions prepared at 5 °C, 20 °C and 40 °C, respectively. C_{70} crystals with two types of shapes such as rhombohedral and needle shapes were obtained. The ratio of the two shapes depends on the saturated solution. The ratio of rhombohedral crystals was predominant using the saturated solution prepared at a lower temperature of 5 °C, while needle crystals were predominant using the saturated solution prepared at a higher temperature of 40 °C. The rhombohedral crystals which are stable and of high quality were used in this work. Regardless of the size and number of rhombohedral crystals, they had the same crystal structure and chemical composition.

The chemical composition of the solution-grown C_{70} crystals with rhombohedral shapes was confirmed by FT-IR spectroscopy. Fig. 2(a) shows the FT-IR spectra around 600–1500 cm^{-1} for the solution-grown crystals after drying in air for one day and after annealing at 100 °C under 3.0–4.0 × 10^{-3} Pa for 11 days. The FT-IR spectra of *m*-xylene used as the solvent and the sublimation-grown C_{70} crystals including no solvent are also shown in the figure. Many peaks in the solution-grown C_{70} crystals are observed in the sublimation-grown C_{70} crystals, which are associated with the vibrational modes of the C_{70} molecules.[26,27] In contrast, some peaks indicated by filled triangles in Fig. 2(a) are not observed in the sublimation-grown C_{70} crystals but correspond to those in *m*-xylene. These peaks are associated with the vibrational modes of *m*-xylene. The solution-grown C_{70} crystals thus comprise C_{70} and *m*-xylene, which suggests a solvated structure.

The FT-IR peaks of the solution-grown crystals were shifted by 2–4 cm^{-1} compared to those of the sublimation-grown crystals and *m*-xylene. The slight shift reflects the intermolecular interaction between the C_{70} molecules and the *m*-xylene molecules, as previously reported for C_{60} solvated crystals.[28] In addition, the FT-IR peaks in the solution-grown crystals composed of C_{70} and *m*-xylene remained almost unchanged even after annealing at 100 °C in a vacuum. This indicates that

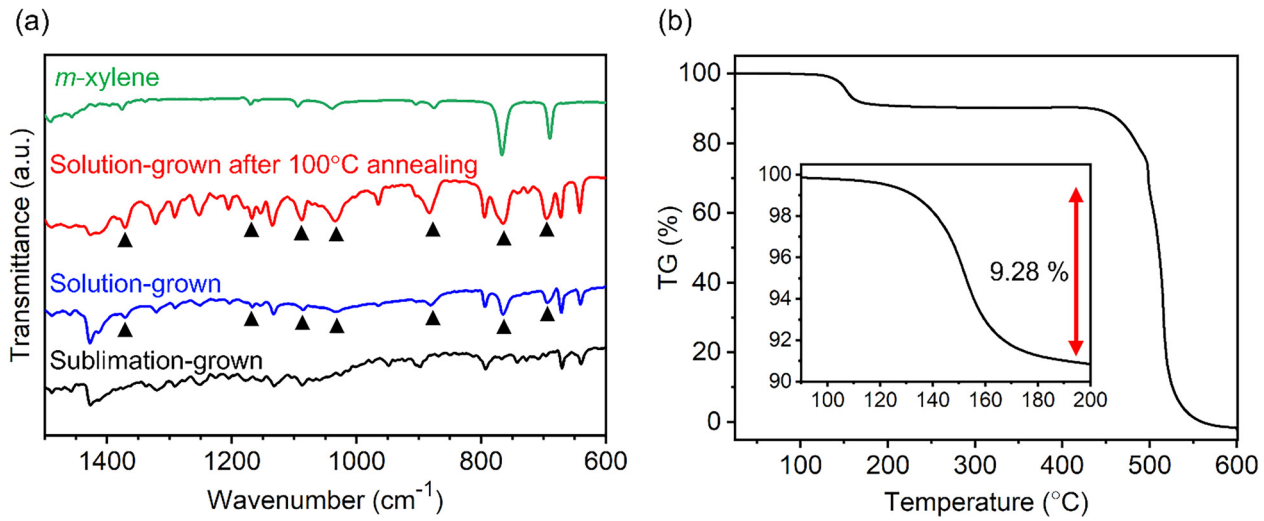

Fig. 2 (a) Blue and red lines show the FT-IR spectra after drying C_{70} crystals with rhombohedral shapes grown from a C_{70}-*m*-xylene solution in air for one day and after annealing them at 100 °C for 11 days under 3.0–4.0 × 10^{-3} Pa, respectively. For reference, the FT-IR spectra of sublimation-grown C_{70} crystals without a solvent and *m*-xylene as the solvent are also shown in the figure. The peaks corresponding to those of *m*-xylene are indicated by filled triangles. (b) TG curve of C70 crystals with rhombohedral shapes grown from C_{70}-*m*-xylene solution. The inset shows an enlarged view in the temperature range from 90 °C to 200 °C. The TG curve was recorded at a heating rate of 10 °C min^{-1} in air.

the solvated structures of C_{70} and *m*-xylene were preserved under the annealing conditions used in this study.

TG measurements were performed to better understand the chemical composition of the solution-grown C_{70} crystals with rhombohedral shapes. Fig. 2(b) shows the TG curves of the solvated C_{70} crystals in air. Weight losses were observed at 140–165 °C and 491–532 °C, which can be related to the desorption of *m*-xylene and sublimation of C_{70} molecules, in the solvated C_{70} crystals, respectively. The desorption temperature of 140–165 °C of *m*-xylene is consistent with the fact that the *m*-xylene-solvated structure is retained even upon annealing at 100 °C as is evident in the FT-IR spectra of Fig. 2(a).

The weight loss corresponding to the desorption of *m*-xylene was approximately 9.28% (Fig. 2(b)). Assuming the aforementioned weight loss and molecular weights of 840.77 and 106.17 of C_{70} and *m*-xylene, respectively, the composition ratio of C_{70} and *m*-xylene in the solvated C_{70} crystals with rhombohedral shapes is estimated to be approximately 10 : 8. The composition ratio was similar to that of solvated C_{70} needle crystals grown by the liquid–liquid interfacial precipitation method with two types of solvents, *m*-xylene and IPA, as reported previously.[23,29] This indicates that the crystal morphology changes considerably depending on the growth method, even if the crystals have almost the same solvent composition ratio. The slight discrepancy in the solvation ratio could be related to crystal morphologies, such as needle and rhombohedral shapes.

The XRD patterns of the solution-grown C_{70} crystals with rhombohedral shapes are shown in Fig. 3. For reference, the XRD pattern of the sublimation-grown C_{70} crystals is also shown in this figure. The PXRD pattern of the sublimation-grown crystals can be explained in terms of two types of crystal forms: the rhombohedral form with a = 10.15 Å and c = 27.95 Å and the hexagonal form with a = 10.16 Å and c = 18.6 Å.

The difference between the two crystal forms is related to changes in the stacking order of the crystal planes. These crystal forms are also in good agreement with those previously reported.[30–32]

The pattern of solution-grown C_{70} crystals with rhombohedral shapes is clearly different from that of sublimation-grown C_{70} crystals. It is assigned to the hexagonal structure with lattice constants of a = 50.3013 Å and c = 24.5686 Å. This was also confirmed by SCXRD measurements. Notably, the XRD pattern remains unchanged even after annealing at 100 °C. This indicates that the hexagonal solvated structure is maintained even after annealing at 100 °C. Thus, the behavior of the XRD pattern is consistent with that of the FT-IR and TG results.

Directly grown C_{70} crystal FETs

Fig. 4(a) shows an SEM image of a C_{70} single crystal with rhombohedral shapes grown directly on the FET substrate (direct-growth C_{70} crystal FETs), which was used for the FET measurements in this study. The channel length L and the channel width W of the FET are estimated to be 23.1 μm and 26.1 μm, respectively (Fig. 4(a)).

An optical microscopy (OM) image of the direct-growth C_{70} crystal FET is shown in Fig. S6 (ESI†). 75% of the obtained

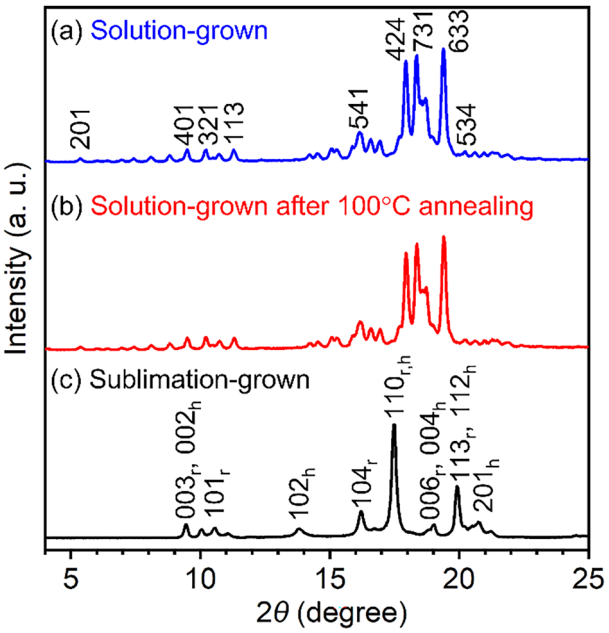

Fig. 3 PXRD patterns of C_{70} crystals with rhombohedral shapes grown from C_{70}-*m*-xylene solution. (a) and (b) XRD patterns after drying them in air for one day and after annealing them at 100 °C for 11 days under 3.0–4.0 × 10^{-3} Pa, respectively. As a reference, the XRD patterns of sublimation-grown C_{70} crystals without the solvent is also shown as (c) in the figure. The XRD pattern of sublimation-grown C_{70} crystals is understood by using those in two kinds of crystal forms such as rhombohedral (denoted as r) and hexagonal (denoted as h) forms.

rhombohedral crystals were grown to bridge the two electrodes on the substrate. In addition, the growth direction to bridge the two electrodes was always a defined crystallographic direction as shown in Fig. 4(a) and Fig. S6 (ESI†). The size distribution of the C_{70} crystals grown to bridge the two electrodes is shown in Fig. S7(a) and (b) (ESI†), where the sizes correspond to the diagonal lengths (short and long) in the obtained crystal morphology as shown in Fig. S7(c) (ESI†). The short diagonal length, which corresponds to the bridge between the two electrodes, was relatively uniform with a size of 51.0 ± 8.80 μm. For FET measurements, some rhombohedral crystals that bridged the two electrodes securely were left on the substrate, while others that bridged the two electrodes fairly well were removed from the substrate. To evaluate mobility, the channel width (W) of all residual crystals bridging the two electrodes was measured from SEM images, as shown in Fig. 4(a).

Fig. 4(b) shows the output characteristics of the vacuum-dried FET. The source–drain current (I_{DS}) increases linearly with the source–drain voltage (V_{DS}) up to approximately V_{DS} = 15 V and approaches a constant maximum value. The transfer characteristics at V_{DS} = 40 V also exhibit good gate modulation with respect to the gate voltage (V_G) (Fig. 4(c)). The output and transfer characteristics show typical n-type FET behavior. Analysis of the transfer characteristics at V_{DS} = 40 V (Fig. 4(c)) shows that the electron mobility (μ), threshold voltage (V_T) and on/off ratio (I_{on}/I_{off}) of the direct growth C_{70} crystal FET are estimated to be 1.19 × 10^{-3} cm^2 V^{-1} s^{-1}, 15.9 V, and 39.6, respectively.

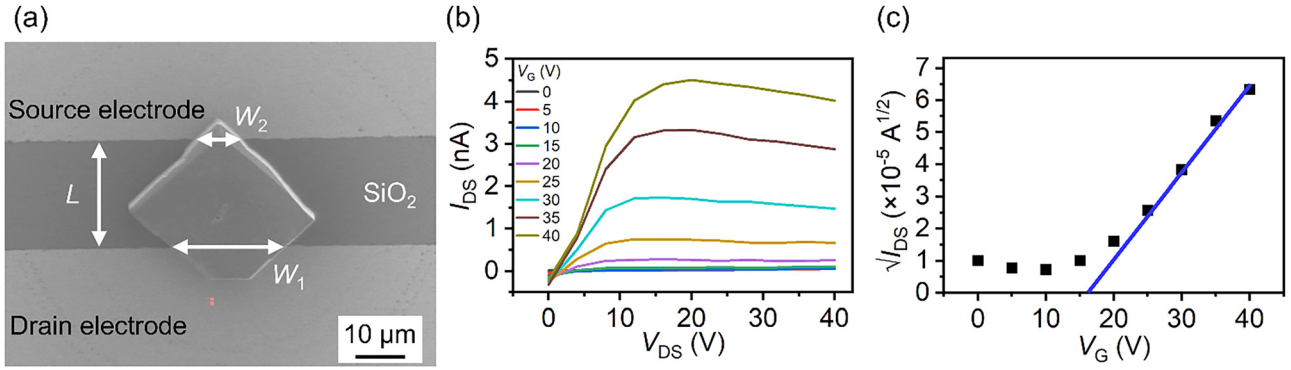

Fig. 4 (a) SEM image of a C_{70} crystal with a rhombohedral shape grown directly on and the electrode FET substrate from a C_{70}-*m*-xylene solution. Typical (b) output and (c) transfer characteristics of direct growth C_{70} crystal FETs before annealing in a vacuum, as measured at 27 °C.

Thus, the transport properties of the direct-growth C_{70} crystal FETs were successfully characterized.

The transport properties of C_{60} and C_{70} crystals are known to deteriorate significantly due to the adsorption of H_2O and O_2 in the crystals; however, these species can be desorbed by annealing at approximately 100 °C.[33,34] To remove the H_2O and O_2 adsorbed in the C_{70} crystals, the FET devices were annealed at 100 °C under 3.0–4.0 × 10^{-3} Pa for 25 days. Notably, the *m*-xylene in the solvated C_{70} crystals remains in the crystals even after vacuum-annealing at 100 °C, as the desorption of *m*-xylene requires a higher temperature of 140–165 °C, as shown in the FT-IR and TG results. The electron mobility in the direct growth C_{70} crystal FETs increased significantly by vacuum-annealing at 100 °C. This indicates that the increase in electron mobility is attributed to the desorption of H_2O and O_2 by vacuum-annealing at 100 °C, as previously reported for C_{60} and C_{70} crystals.[7,23]

In addition, the effect of *m*-xylene in the solvated crystals is of interest for higher mobility. Evaporation of the solvent by heat-treatment at a higher temperature of 200 °C could lead to experimental evidence of solvent effects for solvated crystal FETs. However, heat treatment not only evaporates the solvent but also leads to the degradation of crystallinity with a change in the crystal structure as has already been observed for C_{70} needle crystals.[23] Therefore, it is difficult to accurately measure the solvent effect or pure C_{70} crystal FETs.

Fig. 5(a) shows the relationship between the electron mobility of the directly grown C_{70} crystal FETs and the number of days they were annealed at 100 °C in a vacuum, where the values of the electron mobilities were measured at 100 °C. The electron mobility increased and approached a constant maximum value as the number of days of annealing increased. The maximum value of mobility was 1.50 cm^2 V^{-1} s^{-1} after 25 days of annealing at 100 °C.

It is assumed that the mobility value reaches a constant maximum value after 25 days of annealing, although further annealing could lead to a slight increase in mobility. In fact, the dependence of the slope $\left(\partial\sqrt{I_{DS}}/\partial V_G\right)$ of the transfer characteristics, which is used to evaluate the mobility, on the number of annealing days was well-fitted with an exponential curve as shown in Fig. S8 (ESI†). After fitting, the constant maximum value of mobility is evaluated as 1.59 cm^2 V^{-1} s^{-1}, which is slightly higher than the value after 25 days of annealing. A similar behavior of mobility as a function of the number of days of annealing was also observed for other samples with rhombohedral crystals. The saturation of mobility occurs in all samples after more than 20 days of annealing, where O_2 and H_2O in the crystals are completely removed by annealing. The

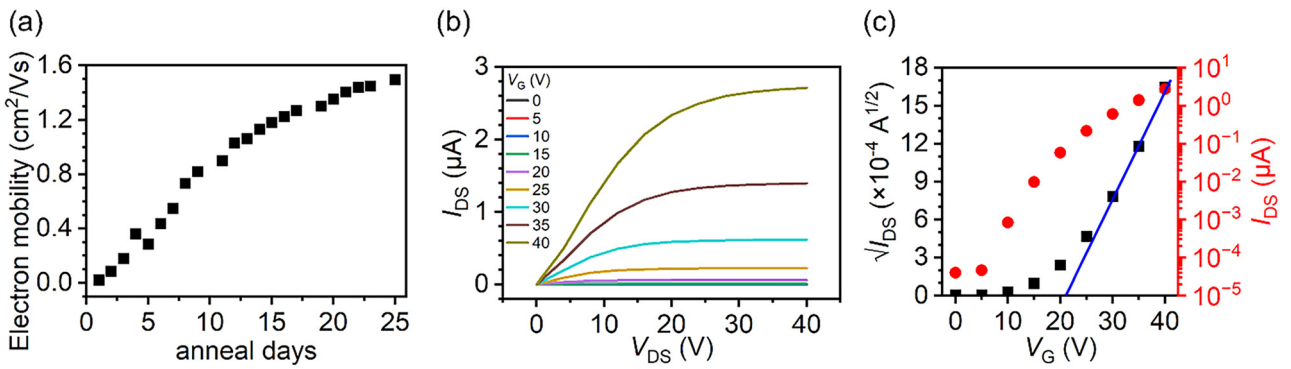

Fig. 5 (a) Increase in the electron mobility of direct growth C_{70} crystal FETs as a function of the number of days they were annealed at 100 °C under 3.0–4.0 × 10^{-3} Pa. Vacuum annealing leads to the desorption of H_2O and O_2 absorbed in the crystals. Typical (b) output and (c) transfer characteristics of direct growth C_{70} crystal FETs after annealing at 100 °C under 3.0–4.0 × 10^{-3} Pa for 25 days, as measured at 27 °C.

Table 1 Comparison of the electrical properties of fullerene-based OFETs reported to date

		Configuration	μ ($cm^2\ V^{-1}\ s^{-1}$)	V_T (V)	I_{on}/I_{off}	Ref.
C_{60}	Thin film	Bottom contact	8.00×10^{-2}	15.0	1.09×10^6	1
			5.60×10^{-1}	17.0	$>10^8$	3
			6.50×10^{-1}	32.0	$>10^6$	4
			2.00×10^{-1}	—	—	5
			3.23	17.1	4.00×10^6	6
		Top contact	4.90	—	—	12
			6.00	—	—	5
			4.30	<1.00	$>10^6$	13
	Crystal	Bottom contact	3.00×10^{-2}	3.30×10^{-1}	1.35×10^2	7
			2.00×10^{-2}	0	—	8
			$\sim 10^{-2}$	−13.0	$\sim 10^2$	9
			2.00×10^{-3}	—	—	10
			3.82×10^{-2}	—	—	11
		Top contact	11.1	28.0	2.50×10^6	14
			2.00 ± 0.61	36.0 ∼ 85.0	$>10^6$	15
			2.30	16.5	2.40×10^4	16
			5.09	6.60×10^{-1}	10^5–10^6	17
C_{70}	Thin film	Bottom contact	2.00×10^{-3}	27.0	—	2
			6.60×10^{-2}	40.0	$>10^5$	4
	Crystal	Bottom contact	6.00×10^{-5}	—	—	22
			1.32×10^{-2}	9.64	64.0	23
			8.20×10^{-5}	—	—	20
			$\sim 10^{-5}$	—	—	21
			1.14	17.2	7.84×10^4	This work

evaporation rate of O_2 and H_2O is high in smaller crystals as the specific surface area is large in smaller crystals. More than 20 days of annealing for rhombohedral crystals is clearly longer than 9 days for smaller needle crystals reported previously.[23] Thus, the days of annealing leading to mobility saturation depend on the crystal size, *i.e.*, the specific surface area.

Fig. 5(b) and (c) show the output and transfer characteristics of the direct growth C_{70} crystal FETs at 27 °C after annealing at 100 °C under 3.0–4.0 $\times 10^{-3}$ Pa for 25 days. The current values of the μA orders increase sharply compared to the nA orders before annealing as shown in Fig. 4(b). According to previous studies on C_{70} needle-crystal FETs with poor electrical contact between crystals and electrodes, in the output characteristics, I_{DS} increased non-linearly and slowly with V_{DS} in the low voltage range.[25] In addition, no current saturation was observed even at high V_{DS}. This behavior may be attributed to poor contact or non-ohmic contact between the C_{70} crystal and the FET substrate with the electrodes. In the direct-growth C_{70} crystal FETs measured in this study, the non-ohmic behavior was largely improved so that ideal and excellent output characteristics, including the linear and saturation regions, were clearly observed (Fig. 5(b)). The electron mobility, V_T and I_{on}/I_{off} of the direct growth C_{70} crystal FETs after annealing are estimated to be 1.14 $cm^2\ V^{-1}\ s^{-1}$, 21.1 V and 6.75 $\times 10^4$, respectively, as measured at 27 °C. The electron mobility increased by three orders of magnitude compared to that before annealing.

The electron mobility, V_T, and I_{on}/I_{off} for fullerene-based OFETs with C_{60} are summarized in Table 1. The electron mobility of the direct-growth C_{70} crystal FETs measured in this study exhibits the highest value compared to those of OFETs based on C_{70} as previously reported.[20–23] The electron mobility value is also comparable to that of top-contact C_{60} based FETs, which correspond to the highest performance in n-type OFETs.

The electron mobility values after annealing for 25 days were 1.50 $cm^2\ V^{-1}\ s^{-1}$ at 100 °C and 1.14 $cm^2\ V^{-1}\ s^{-1}$ at 27 °C, indicating that the mobility increases with temperature. This behaviour suggests that electron transport in the C_{70} crystals follows a hopping conduction mechanism associated with thermal activity, which is a typical conduction mechanism in molecular crystals.

In previous studies on C_{70} needle-crystal FETs, the electron mobility was estimated from the transfer characteristics, assuming negligible contact resistance between the C_{70} crystal and the S/D electrodes on the substrate. However, if the contact resistance is significant, this may result in reduced current values, possibly leading to an underestimation of electron mobility. In contrast, in this study, the contact was significantly improved, minimizing the limit of the injection current and allowing a more accurate estimation of the intrinsic electron mobility.

Conclusions

In this study, high-mobility FETs fabricated by the direct growth of C_{70} crystals from C_{70} saturated *m*-xylene solution have been demonstrated. Good electrical contact between the C_{70} crystals and FET substrates was realized with electrodes in the bottom-gated bottom-contact FET configuration. The C_{70} crystals obtained exhibit rhombohedral shapes with solvated hexagonal structures. Directly grown C_{70} crystal FETs exhibit typical n-type output and transfer characteristics. The electron mobility increases with annealing at 100 °C in a vacuum, leading to the desorption of H_2O and O_2 in the crystals, although solvation in the crystals is maintained. The solvated C_{70} crystal FETs have a high electron mobility of 1.14 $cm^2\ V^{-1}\ s^{-1}$ which is an improvement of more than two orders of magnitude compared to the previously reported

C_{70} FETs. The electron mobility value was also comparable to that of the electron mobility in top-contact C_{60} based FETs, which corresponds to the highest mobility in n-type OFETs. This shows the potential application of C_{70} crystals in electronic devices. It is anticipated that more advanced solution-processing techniques developed for organic crystalline FETs[24,25] will be employed in the fabrication of high-mobility C_{70} FETs for practical applications.

Author contributions

Yuto Sakai: data curation, formal analysis, investigation, methodology, validation, visualization, writing review, and editing. Taiyo Araki: data curation, formal analysis, investigation, methodology, validation, visualization, writing review, and editing. Ryo Suzuki: data curation, formal analysis, funding acquisition, visualization, writing review, and editing. Toshiyuki Sasaki: data curation, formal analysis, visualization, writing review, and editing. Kouhei Ichiyanagi: data curation, formal analysis, visualization, writing review, and editing. Tadahiko Hirai: formal analysis, visualization, writing review, and editing. Nobuyuki Aoki: resources (FET devices), writing review, and editing. Masaru Tachibana: conceptualization, project administration, supervision, funding acquisition, writing – original draft, writing – review, and editing.

Conflicts of interest

There are no conflicts to declare.

Data availability

The data supporting this article have been included as part of the ESI.†

Acknowledgements

We thank Mr Ken Inoue from Yokohama City University for his assistance in the preparation of this manuscript. We also thank Prof. Genji Kurisu, Dr Takanori Nakane, and Dr Akihiro Kawamoto from the Institute for Protein Research, Osaka University, Dr Naruhiko Adachi from the University of Tsukuba, Dr Yusuke Yamada from Tohoku University, and Dr Haruki Sugiyama from the Comprehensive Research Organization for Science and Society. The XRD measurements were performed at BL40XU and BL41XU at SPring-8 with the approval of JASRI (Proposal no. 2023B2429, 2023B2432, 2024A1112, and 2024 A1142). This work was supported by PRESTO, Japan Science and Technology Agency (JPMJPR1995), and Japan Society for the Promotion of Science (JSPS) KAKENHI Grants-in-Aid for Scientific Research (Grant No. 19K23579, 23H01305, 23K26000, and 25K08281). This research was partially supported by the Research Support Project for Life Science and Drug Discovery (Basis for Supporting Innovative Drug Discovery and Life Science Research (BINDS)) from AMED under Grant Number JP24ama121001 (support number 6707).

References

1 R. C. Haddon, A. S. Perel, R. C. Morris, T. T. M. Palstra, A. F. Hebard and R. M. Fleming, *Appl. Phys. Lett.*, 1995, **67**, 121–123.
2 R. C. Haddon, *J. Am. Chem. Soc.*, 1996, **118**, 3041–3042.
3 S. Kobayashi, T. Takenobu, S. Mori, A. Fujiwara and Y. Iwasa, *Appl. Phys. Lett.*, 2003, **82**, 4581–4583.
4 J. N. Haddock, X. Zhang, B. Domercq and B. Kippelen, *Org. Electron.*, 2005, **6**, 182–187.
5 T. D. Anthopoulos, B. Singh, N. Marjanovic, N. S. Sariciftci, A. M. Ramil, H. Sitter, M. Cölle and D. M. de Leeuw, *Appl. Phys. Lett.*, 2006, **89**, 213504.
6 M. Kitamura, S. Aomori, J. H. Na and Y. Arakawa, *Appl. Phys. Lett.*, 2008, **93**, 033313.
7 A. L. Briseno, S. C. B. Mannsfeld, M. M. Ling, S. Liu, R. J. Tseng, C. Reese, M. E. Roberts, Y. Yang, F. Wudl and Z. Bao, *Nature*, 2006, **444**, 913–917.
8 K. Ogawa, T. Kato, A. Ikegami, H. Tsuji, N. Aoki, Y. Ochiai and J. P. Bird, *Appl. Phys. Lett.*, 2006, **88**, 112109.
9 Y. Ochiai, K. Ogawa, N. Aoki and J. P. Bird, *J. Phys.:Conf. Ser.*, 2009, **159**, 012004.
10 D. Mahdaoui, C. Hirata, K. Nagaoka, K. Miyazawa, K. Fujii, T. Ando, M. Abderrabba, O. Ito, M. Takagi, T. Ishimoto, M. Tachikawa, S. Yagyu, Y. Liu, Y. Nakajima, Y. Nemoto, K. Tsukagoshi and T. Wakahara, *J. Mater. Chem. C*, 2022, **10**, 3770–3774.
11 T. Wakahara, C. Hirata, D. Mahdaoui, K. Fujii, Y. Matsushita, O. Ito, M. Takagi, T. Shimazaki, M. Tachikawa, S. Yagyu, Y. Liu, Y. Nakajima, T. Nagai and K. Tsukagoshi, *Carbon*, 2025, **233**, 119838.
12 K. Itaka, M. Yamashiro, J. Yamaguchi, M. Haemori, S. Yaginuma, Y. Matsumoto, M. Kondo and H. Koinuma, *Adv. Mater.*, 2006, **18**, 1713–1716.
13 X. H. Zhang and B. Kippelen, *J. Appl. Phys.*, 2008, **104**, 104504.
14 H. Li, B. C. K. Tee, J. J. Cha, Y. Cui, J. W. Chung, S. Y. Lee and Z. Bao, *J. Am. Chem. Soc.*, 2012, **134**, 2760–2765.
15 H. Li, C. Fan, M. Vosgueritchian, B. C.-K. Tee and H. Chen, *J. Mater. Chem. C*, 2014, **2**, 3617–3624.
16 X. Zhao, T. Liu, Y. Cui, X. Hou, Z. Liu, X. Dai, J. Kong, W. Shi and T. J. S. Dennis, *Nanoscale*, 2018, **10**, 8170–8179.
17 Z. Lu, W. Deng, X. Fang, J. Xiao, B. Lu, X. Zhang, A. A. A. Pirzado, J. Jie and X. Zhang, *Adv. Funct. Mater.*, 2021, **31**, 2105459.
18 P. Hu, X. He and H. Jiang, *InfoMat*, 2021, **3**, 613–630.
19 S. Arabnejad, A. Pal, K. Yamashita and S. Manzhos, *Front. Energy Res.*, 2019, **7**, 00003.
20 T. Wakahara, K. Nagaoka, C. Hirata, K. Miyazawa, K. Fujii, Y. Matsushita, O. Ito, M. Takagi, T. Shimazaki, M. Tachikawa, Y. Wada, S. Yagyu, Y. Liu, Y. Nakajima and K. Tsukagoshi, *RSC Adv.*, 2022, **12**, 19548–19553.

21 D. Mahdaoui, C. Hirata, K. Nagaoka, K. Miyazawa, K. Fujii, T. Ando, M. Abderrabba, O. Ito, S. Yagyu, Y. Liu, Y. Nakajima, K. Tsukagoshi and T. Wakahara, *Nanomaterials*, 2023, **13**, 2469.
22 D. Mahdaoui, C. Hirata, K. Nagaoka, K. Miyazawa, K. Fujii, T. Ando, Y. Matsushita, M. Abderrabba, O. Ito, K. Tsukagoshi and T. Wakahara, *Diamond Relat. Mater.*, 2022, **128**, 109217.
23 Y. Mitake, A. Gomita, R. Yamamoto, M. Watanabe, R. Suzuki, N. Aoki, M. Tanimura, T. Hirai and M. Tachibana, *Chem. Phys. Lett.*, 2022, **807**, 140094.
24 S. Chen, Z. Li, Y. Qiao and Y. Song, *J. Mater. Chem. C*, 2021, **9**, 1126–1149.
25 Z. Chen, S. Duan, X. Zhang and W. Hu, *Mater. Chem. Front.*, 2024, **8**, 2227–2272.
26 R. A. Jishi, M. S. Dresselhaus, G. Dresselhaus, K. A. Wang, P. Zhou, A. M. Rao and P. C. Eklund, *Chem. Phys. Lett.*, 1993, **206**, 187–192.
27 K. Thirunavukkuarasu, V. C. Long, J. L. Musfeldt, F. Borondics, G. Klupp, K. Kamarás and C. A. Kuntscher, *J. Phys. Chem. C*, 2011, **115**, 3646–3653.
28 Y. Funamori, R. Suzuki, T. Wakahara, T. Ohmura, E. Nakagawa and M. Tachibana, *Carbon*, 2020, **169**, 65–72.
29 M. Watanabe, A. Gomita, R. Suzuki and M. Tachibana, *Carbon Trends*, 2023, **10**, 100246.
30 M. A. Verheijen, H. Meekes, G. Meijer, P. Bennema, J. L. de Boer, S. van Smaalen, G. van Tendeloo, S. Amelinckx, S. Muto and J. van Landuyt, *Chem. Phys.*, 1992, **166**, 287–297.
31 G. B. M. Vaughan, P. A. Heiney, D. E. Cox, J. E. Fischer, A. R. McGhie, A. L. Smith, R. M. Strongin, M. A. Cichy and A. B. Smith, *Chem. Phys.*, 1993, **178**, 599–613.
32 J. Janaki, G. V. N. Rao, V. S. Sastry, Y. Hariharan, T. S. Radhakrishnan, C. S. Sundar, A. Bharati, M. C. Valsakumar and N. Subramanian, *Solid State Commun.*, 1995, **94**, 37–40.
33 T. Arai, Y. Murakami, H. Suematsu, K. Kikuchi, Y. Achiba and I. Ikemoto, *Solid State Commun.*, 1992, **84**, 827–829.
34 A. Tapponnier, I. Biaggio and P. Günter, *Appl. Phys. Lett.*, 2005, **86**, 112114.

